Article

New Insights into the Photocatalytic Properties of RuO$_2$/TiO$_2$ Mesoporous Heterostructures for Hydrogen Production and Organic Pollutant Photodecomposition

Md. Tamez Uddin,[†] Odile Babot,[†] Laurent Thomas,[†] Céline Olivier,[†] Matteo Redaelli,[‡]
Massimiliano D'Arienzo,[‡] Franca Morazzoni,[‡] Wolfram Jaegermann,[§] Nils Rockstroh,[∥] Henrik Junge,[∥]
and Thierry Toupance*,[†]

[†]Univ. Bordeaux, Institut des Sciences Moléculaires, UMR 5255 CNRS, 351 Cours de la Libération, F-33405 Talence Cedex, France
[‡]INSTM, Department of Materials Science, University of Milano-Bicocca, Via R. Cozzi 53, I-20125 Milano, Italy
[§]Institute of Material Science, Technische Universität Darmstadt, Petersenstraße 23, D-64287 Darmstadt, Germany
[∥]Leibniz Institute for Catalysis, University of Rostock, Albert-Einstein-Straße 29a, D-18059 Rostock, Germany

S *Supporting Information*

ABSTRACT: Photocatalytic activities of mesoporous RuO$_2$/TiO$_2$ heterojunction nanocomposites for organic dye decomposition and H$_2$ production by methanol photoreforming have been studied as a function of the RuO$_2$ loading in the 1–10 wt % range. An optimum RuO$_2$ loading was evidenced for both kinds of reaction, the corresponding nanocomposites showing much higher activities than pure TiO$_2$ and commercial reference P25. Thus, 1 wt % RuO$_2$/TiO$_2$ photocatalyst led to the highest rates for the degradation of cationic (methylene blue) and anionic (methyl orange) dyes under UV light illumination. To get a better understanding of the mechanisms involved, a comprehensive investigation on the photogenerated charge carriers, detected by electron spin resonance (ESR) spectroscopy in the form of O$^-$, Ti^{3+}, and O$_2^-$ trapping centers, was performed. Along with the key role of superoxide paramagnetic species in the photodecomposition of organic dyes, ESR measurements revealed a higher amount of trapped holes in the case of the 1 wt % RuO$_2$/TiO$_2$ photocatalyst that allowed rationalizing the trends observed. On the other hand, a maximum average hydrogen production rate of 618 μmol h^{-1} was reached with 5 wt % RuO$_2$/TiO$_2$ photocatalyst to be compared with 29 μmol h^{-1} found without RuO$_2$. Favorable band bending at the RuO$_2$/TiO$_2$ interface and the key role of photogenerated holes have been proposed to explain the highest activity of the RuO$_2$/TiO$_2$ photocatalysts for hydrogen production. These findings open new avenues for further design of RuO$_2$/TiO$_2$ nanostructures with a fine-tuning of the RuO$_2$ nanoparticle distribution in order to reach optimized vectorial charge distribution and enhanced photocatalytic hydrogen production rates.

Maximum H$_2$ production with **5%RuO$_2$/TiO$_2$** photocatalyst
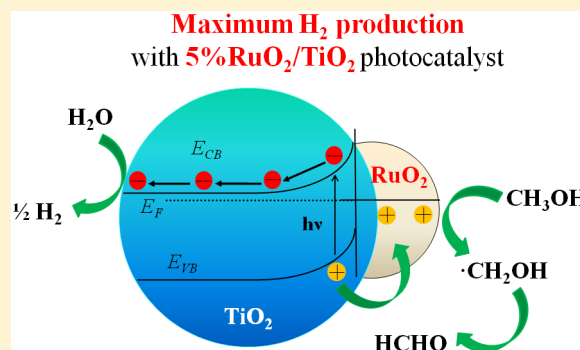
1. INTRODUCTION

Environmental issues along with the continuous energy demand increase arising from the global population growth require the development of advanced technologies addressed toward the production of green fuels or the efficient elimination of harmful pharmaceutical or organic pollutants. In this context, semiconductor heterogeneous photocatalysis appeared to be a versatile concept for green technology[1,2] and was directed to a wide range of purposes as hydrogen production, C–C bond formation, carbon dioxide remediation, and depollution.[3] So far, titanium dioxide (TiO$_2$) is the best understood prototype of metal oxide semiconductor for photocatalytic applications due to both fundamental and practical reasons such as good biological and chemical stabilities, low cost, nontoxicity, and long-term stability against photocorrosion and chemical corrosion, combined with rather high photocatalytic efficien-

cies.[1,4] Nevertheless, the use of this metal oxide suffers from some limitations related to fast recombination phenomena of photoinduced electron–hole pairs during the photocatalytic processes. In this context, different strategies have been investigated to lower the recombination rate of electron–hole pairs by designing metal/metal oxide (Ag/TiO$_2$[5,6] or Au/TiO$_2$[7,8]), n-type metal oxide/n-type metal oxide (SnO$_2$–TiO$_2$)[9,10] or p-type metal oxide/n-type metal oxide (NiO-TiO$_2$)[11,12] heterostructure nanocatalyts. Such heterojunctions favor charge separation through an easy transfer of electrons or holes from one material to the other, depending upon the band alignment at the interface.[13]

Belonging to the family of transition metal oxides with rutilelike structure, ruthenium(IV) oxide (RuO_2) shows an intrinsic submetallic property and its Fermi level EF is situated in the partially filled Ru 4d state.[14,15] Moreover, when TiO_2 is put into contact with RuO_2, that has a high work function[16] situated in the band gap above the valence band of TiO_2, hole transfer from TiO_2 to RuO_2 can be expected after irradiation of the nanocomposite. However, no sufficient attention has been paid so far concerning the study and the rationalization of the photocatalytic properties of RuO_2/TiO_2 nanocomposites.[17−20] We have recently reported a thorough study of the band alignment in RuO_2/TiO_2 nanocomposites, which allowed explaining the best photocatalytic properties of this hetero-junction compared to pure TiO_2.[21] Nevertheless, no efforts have been put in the investigation of the RuO_2/TiO_2 nanocomposites in connection to the type, amount, and location of the paramagnetic defects involved in the photo-catalytic processes.

Aiming at addressing these points, we report the study of the photocatalytic activity under UV-light of RuO_2/TiO_2 nano-composites in two different processes: the photodecomposition of organic dyes and the production of hydrogen by methanol photoreforming. Depending upon the nature of the reaction investigated, an optimum RuO_2 loading was determined. To get deeper insight into the photocatalytic mechanism, a compre-hensive investigation of the photogenerated charge carriers, detected by electron spin resonance (ESR) spectroscopy in the form of O^-, Ti^{3+}, and O_2^- trapping centers, was performed. Their abundance was related to the RuO_2 loading and to the photoefficiency of the catalysts. This study may represent a first attempt toward an effective detection of the charge trapping centers involved in the photocatalytic reactions assisted by RuO_2/TiO_2 heterostructures.

2. EXPERIMENTAL METHODS

2.1. Synthesis. RuO_2/TiO_2 heterostructures were prepared by impregnation of anatase TiO_2 nanopowders[22] with a ruthenium(III) salt according to a previously reported procedure.[21] In a typical synthesis experiment, anatase TiO_2 nanopowder (0.3 g) was suspended into a solution of a given amount of ruthenium(III) pentan-2,4-dionate (Alfa Aesar) in tetrahydrofuran (50 mL). After being stirred at room temperature for 4 h, the volatiles were evaporated and the resulting solids were dried at 70 °C overnight. Further calcination at 400 °C in air for 6 h yielded the target RuO_2/TiO_2 catalyst. Samples including 1, 2.5, 5, and 10 wt % of RuO_2 were synthesized by adding 0.0091, 0.023, 0.047, and 0.094 g of ruthenium(III) pentan-2,4-dionate, respectively, to THF (50 mL). The resulting samples are hereafter named 1 wt % RuO_2/TiO_2, 2.5 wt % RuO_2/TiO_2, 5 wt % RuO_2/TiO_2, and 10 wt % RuO_2/TiO_2 nanocomposites.

2.2. Characterization Methods. A Bruker AXS diffrac-tometer (D2 PHASER A26-X1-A2B0D3A) including a Cu anode ($K\alpha$ radiation) and a Micromeritics ASAP2010 were used to record X-ray diffraction (XRD) patterns and nitrogen adsorption−desorption isotherms respectively, according to previously established procedures.[21,23] X-ray photoelectron spectroscopy experiments were performed at the Darmstadt Integrated System for MATerial research (DAISY-MAT) using previously reported procedures.[24] Transmission electron microscopy (TEM) was carried out using a JEOL JEM 2100F (JEOL, Tokyo, Japan), operating at an acceleration voltage of 200 kV (wavelength λ = 2.51 pm) equipped with a

Schottky-type FEG and an EDS system (Oxford, Wiesbaden, Germany). For the sample preparation, the photocatalyst powders were dispersed in an ultrasonic bath (high purity methanol 99.8%, Sigma−Aldrich), and a small droplet of the suspension was placed on a holey carbon (Cu) grid. ESR investigation was performed by a Bruker EMX spectrometer operating at the X-band frequency and equipped with an Oxford cryostat working in the temperature range of 4−298 K. The nanocrystals were charged into quartz glass tubes connected both to a high vacuum pumping system and to a controlled gas feed (O_2). Spectra were recorded at 130 K in vacuo conditions ($p < 10^{-5}$ mbar), before and after 30 min of UV irradiation inside the ESR cavity either in vacuo ($p < 10^{-5}$ mbar) or in the presence of $p(O_2)$ = 10 mbar. For each sample, the absence of a signal before irradiation was checked. No significant differences resulted between the spectra recorded just before and 20 min after switching off the UV irradiation, except a small decrease of the signal intensity. Spectra were acquired with a modulation frequency of 100 kHz, modulation amplitudes of 5 gauss, and microwave powers of 10 mW. Irradiation was performed by an UV 150 W Xe lamp (Oriel) with the output radiation focused on the samples in the cavity by an optical fiber (50 cm length, 0.3 cm diameter). The gram values were calculated by standardization with α,α'-diphenyl-β-picryl hydrazyl (DPPH). The spin concentration was obtained by double integration of the resonance lines, referring to the area of the standard Bruker weak pitch ($9.7 \times 10^{12} \pm 5\%$ spins cm^{-1}). Accuracy on double integration was $\pm15\%$. Care was taken to always keep the most sensitive part of the ESR cavity (1 cm length) filled. Spectra simulations and fits were performed using SIM 32.[25]

2.3. Photocatalytic Experiment. Photocatalytic activity of the different nanocatalysts was first examined by the degradation of methyl orange (MO) dye (Alfa Aesar, reagent grade, used as supplied) under UV light. All the experiments were conducted at room temperature in a Pyrex beaker open to air illuminated with a 125 W high-pressure mercury lamp (Philips, HPL-N 125 W/542 E27), emitting UV light (365 and 313 nm), positioned above the solution beaker. In a typical experiment, 0.1 g of photocatalyst was immersed in 100 mL of MO aqueous solution (10 mg/L) that corresponds to a catalyst concentration of 1.0 g/L. Prior to irradiation, the suspension was stirred in the dark for 30 min to reach adsorption/desorption equilibrium. Small amounts of dye solution were withdrawn first after dark stirring and afterward in regular time intervals from the reactor and then centrifuged (4000 rpm, 10 min). Monitoring the absorption intensity of MO at 464 nm with a UV−visible Spectrophotometer (Shimadzu, UV-1650 pc) led to the remaining amount of dyes. In all the cases, blank experiments were also conducted with the catalysts in the absence of light and without the catalysts when the solution containing the dissolved dye was illuminated.

Furthermore, the photocatalytic production of hydrogen (H_2) was carried out in an argon atmosphere under exclusion of air. Solvents were distilled under an argon atmosphere or degassed via standard procedures prior to use and stored under argon. Each photocatalytic experiment was conducted in a double-walled thermostatically controlled reaction vessel (at a constant temperature of 25 °C) which was connected via a condenser to an automatic gas buret. In a typical reaction, the double-walled reaction vessel connected to the automatic gas buret was evacuated and flushed with argon three times to remove any other gases. The photocatalysts were introduced as
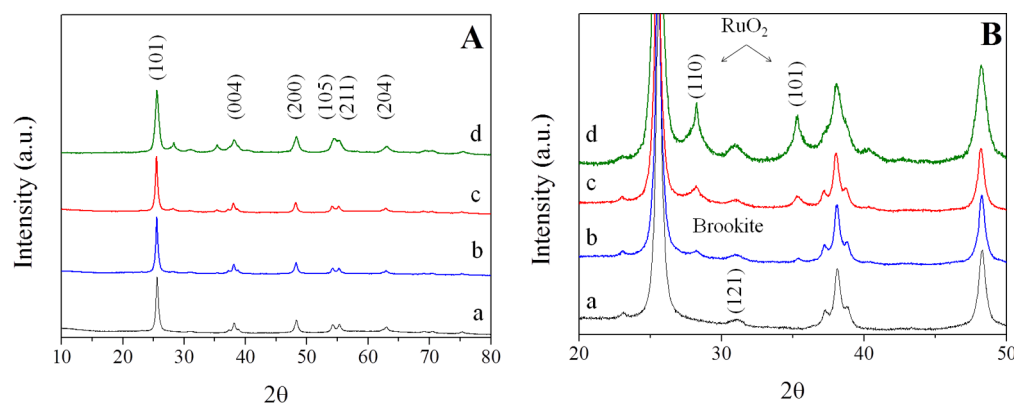
Figure 1. XRD of TiO_2 (a, black), 1 wt % RuO_2/TiO_2 (b, blue), 5 wt % RuO_2/TiO_2 (c, red), and 10 wt % RuO_2/TiO_2 (d, olive) nanomaterials. (A) 2θ region of 10−80° and (B) higher magnification of the 2θ region of 20−50°.

a powder, and the mixture of methanol/H_2O (1:1 v:v, 10 mL) was added; the temperature was maintained at 25 °C. After stirring (300 rpm) for 5 min to reach thermal equilibrium, the photocatalytic reaction was started by irradiating the reaction vessel with UV light (Hg vapor light source (LUMATEC SUPERLITE 400) emitting in the 320−400 nm wavelength range with a power of 1.6 W). The volumes of the evolved gases were determined by an automatic gas buret, equipped with a pressure sensor. The gas evolved was taken and quantitatively analyzed by gas chromatography (HP6890N, carboxen 1000, thermal conductivity detector (TCD) and methanizer/flame ionization detector (FID), external calibration). The variance of the volumes for reproduction of experiments was between 1 and 15%.

3. RESULTS AND DISCUSSION

3.1. Characterization of Nanocatalysts. XRD patterns of TiO_2 and heterostructure RuO_2/TiO_2 nanocatalysts containing different wt % (1.0, 5.0, and 10.0) of RuO_2 exhibited the diffraction lines expected for anatase TiO_2 (JCPDS 21-1272), traces (2−4 wt %) of brookite TiO_2 (JCPDS 29-1360), and rutile RuO_2 (JCPDS 43-1027) (Figure 1). Furthermore, the intensity of the peaks at 28.1 and 35.5 2θ, which are attributed to RuO_2 (110) and (101) planes, increased with the amount of RuO_2 introduced (Figure 1B).

As far as the textural properties are concerned, each sample showed a typical type IV N_2 adsorption−desorption isotherm, including a hysteresis loop which is typical of mesoporous materials, according to the IUPAC classification, as depicted in Figure 2.[26] Increasing the RuO_2 content induced a slight decrease of the specific surface area (S_{BET}) that was found to be 68, 67, 69, 63, and 60 ± 2 $m^2 g^{-1}$ for TiO_2, 1 wt % RuO_2/TiO_2, 2.5 wt % RuO_2/TiO_2, 5 wt % RuO_2/TiO_2, and 10 wt % RuO_2/TiO_2, respectively. Moreover, the presence of a hysteresis loop indicates that each sample contained pores of nonuniform size and shapes that are characteristic of solids consisting of particles crossed by nearly cylindrical channels or made by aggregates (consolidated) or agglomerates (unconsolidated) of spheroidal particles.[27] It is also worth mentioning that the pore size distribution was found to be similar to different RuO_2 loadings, which suggests that the mesoporosity does not depend upon the RuO_2 amount in the 1−10 wt % range (Figure 2, inset).

To confirm the deposition of RuO_2 on the surface of TiO_2, scanning transmission electron (STEM), bright field (BF), and high angle annular dark field (HAADF) experiments were performed. First of all, the TEM image of the RuO_2/TiO_2
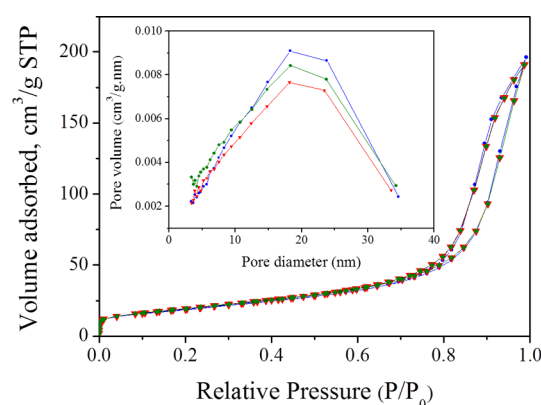

Figure 2. Nitrogen gas adsorption−desorption isotherms and pore-size distribution (inset) of 1 wt % (blue ●), 5 wt % (red ▼), and 10 wt % (olive ◆) RuO_2/TiO_2 photocatalysts.

sample containing 5 wt % RuO_2 was measured. It can be seen that the RuO_2 is deposited as small particles on the surface of TiO_2 nanoparticles (Figure 3A). The BF image (Figure 3B) showed the presence of RuO_2 nanoparticles with a clear contrast in STEM-HAADF image (Figure 3C), indicating the deposition of RuO_2 on the TiO_2 surface. Contrast variation was observed between RuO_2 and TiO_2 nanoparticles because the contrast variation in STEM images is Z-related, and due to the higher atomic number of Ru, those particles are brighter in HAADF images. EDX analysis performed on the sample (Figure 3E) further confirmed the presence of RuO_2 deposited on the surface of TiO_2.

Finally, the surface composition of the RuO_2/TiO_2 nanocomposites was studied by X-ray photoelectron spectroscopy. As previously found for the 1 wt % RuO_2/TiO_2 sample,[21] only the characteristic features of titanium, oxygen, and ruthenium, along with those of adventitious carbon species, were observed in the spectra of the 5 wt % RuO_2/TiO_2 and 10 wt % RuO_2/TiO_2 samples (Figure 4 and Figure S1 of the Supporting Information). The presence of ruthenium was clearly evidenced by the detection of the Ru $3d_{5/2}$ emission line located at 280.55 eV, which is typical of Ru^{4+} cations as expected for RuO_2 (Figure 4B).[28] The high-resolution XPS spectra for Ti 2p yielded binding energies of 464.4 and 458.7 eV assigned to Ti $2p_{1/2}$ and Ti $2p_{3/2}$ core levels, respectively (Figure 4C). The spin−orbit splitting was found to be 5.7 eV, which is in good agreement with the one expected for the Ti^{4+} oxidation state in TiO_2-based nanocomposites.[29] Moreover, no evidence of Ti^{3+}
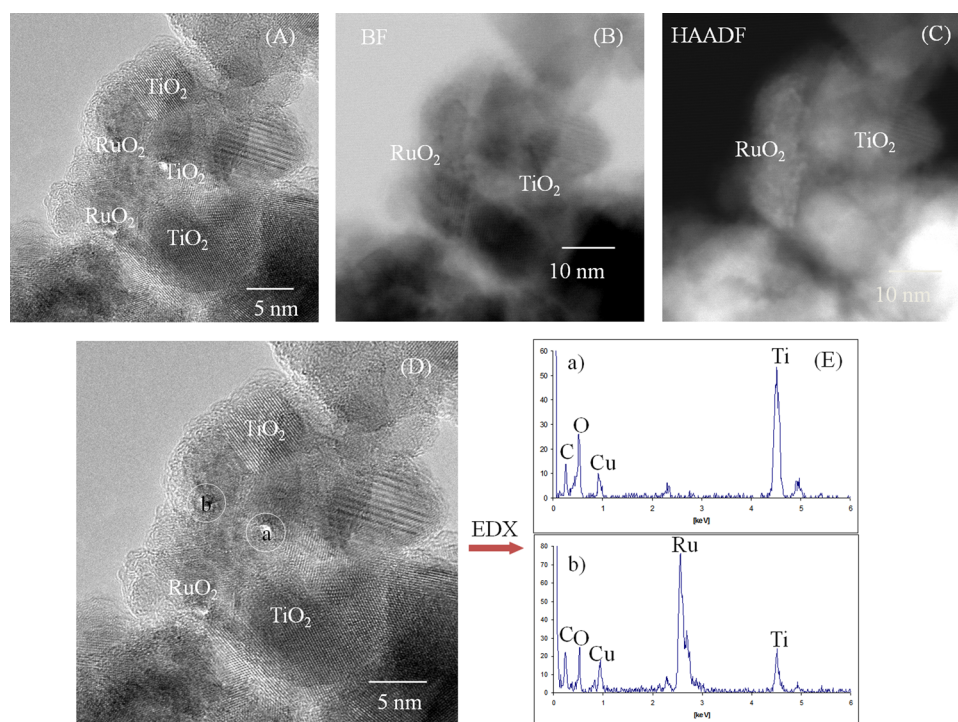
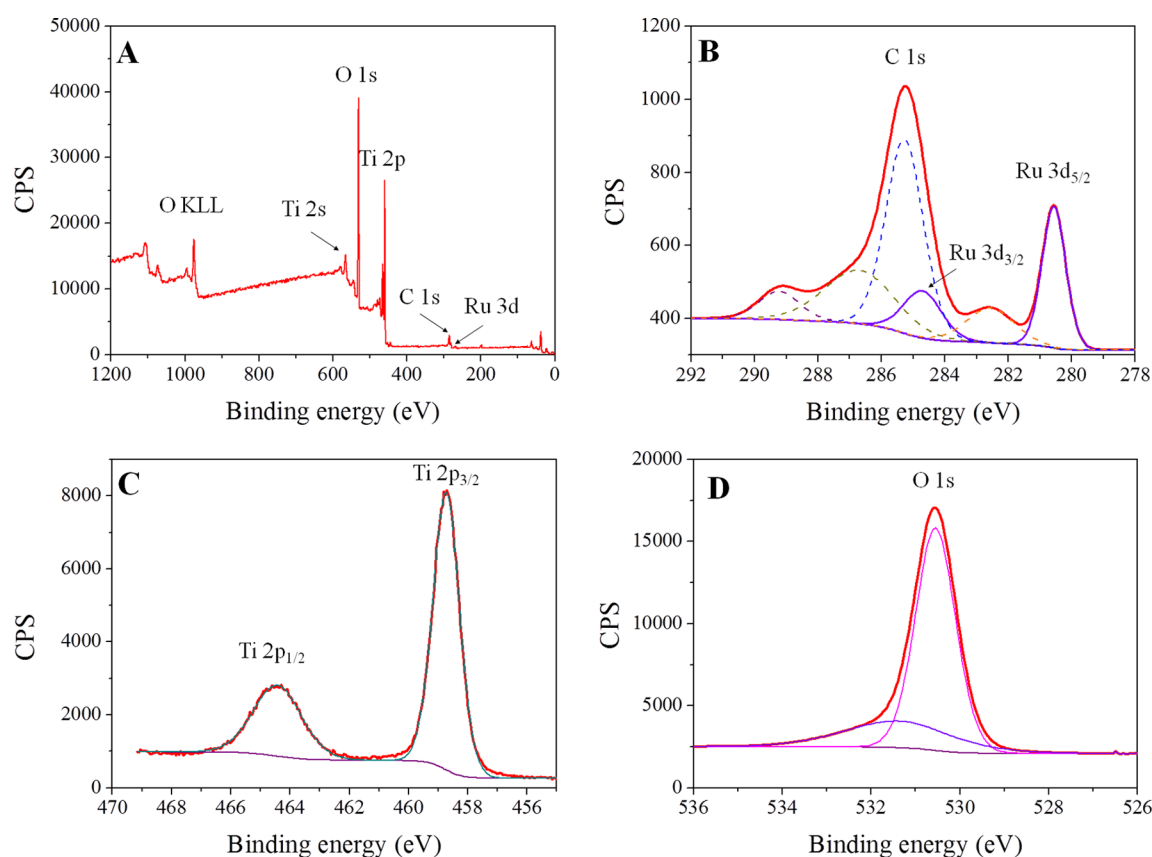**Figure 3.** (A) TEM, (B) STEM-BF, (C) STEM-HAADF images, and (D and E) EDX mapping of 5 wt % RuO$_2$/TiO$_2$ nanoparticles.

Figure 4. (A) XPS survey spectrum for 5 wt % RuO$_2$/TiO$_2$ nanocomposite. (B) High-resolution XPS spectrum of C 1s + Ru 3d after deconvolution for 5 wt % RuO$_2$/TiO$_2$ nanocomposite. (C) High-resolution XPS spectrum of Ti 2p for 5 wt % RuO$_2$/TiO$_2$ nanocomposite. (D) High-resolution XPS spectrum of O 1s after deconvolution for the 5 wt % RuO$_2$/TiO$_2$ nanocomposite.

could be found in the spectrum. Finally, the main component of the O 1s peak located at 530.5 eV was attributed to O−Ti bonds in bulk TiO$_2$, whereas the tailing to higher energies can be related to hydroxylation of TiO$_2$ particles (Figure 4D).
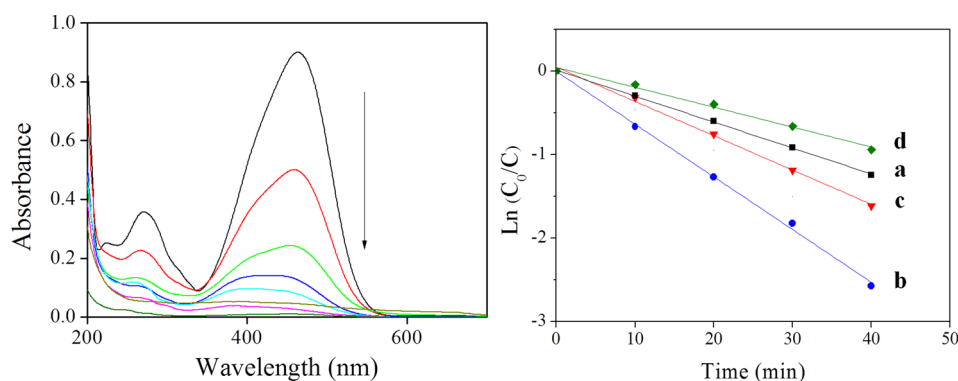
Figure 5. (left) Absorbance changes of MO solution after different irradiation times in the presence of the 1 wt % RuO_2/TiO_2 sample: equilibrium (black), 10 min (red), 20 min (green), 30 min (blue), 40 min (cyan), 50 min (dark yellow), 60 min (magenta), and 80 min (olive). (right) $\ln[C/C_0]$ as a function of the irradiation time for TiO_2 (a, black ■), 1 wt % RuO_2/TiO_2 (b, blue ●), 5 wt % RuO_2/TiO_2 (c, red ▼), and 10 wt % RuO_2/TiO_2 (d, olive ♦) photocatalysts.

As a result, the heterostructures synthesized can be seen as nanocrystalline mesoporous materials made of aggregated networks of anatase TiO_2 and rutile RuO_2 nanoparticles.

3.2. Photocatalytic Activity. To complete our previous study concerning the photocatalytic decomposition of cationic dyes [methylene blue (MB)] with catalytic amounts of RuO_2/TiO_2 nanomaterials,[21] similar experiments were performed with methyl orange (MO) as a typical anionic dye.[30] While MO remained stable under UV irradiation without any catalyst, a progressive decrease in the absorption at 464 nm along with a slight hypsochromic shift were detected upon addition of the nanocatalyst (Figure 5A). Furthermore, the photodegradation of MO by RuO_2/TiO_2 heterojunction nanocatalysts follows a first-order law, $\ln(C/C_0) = -k_{app}t$, where k_{app} is the pseudo first-order rate constant (Figure 5 right, Table 1). As for MB,[21] 1 wt

Table 1. Apparent Rate Constants for the Degradation of MO[a] and MB[b] of TiO2, P25, and RuO2/TiO2 Nanocatalysts

photocatalyst	TiO_2	1 wt % RuO_2/TiO_2	2.5 wt % RuO_2/TiO_2	5 wt % RuO_2/TiO_2	10 wt % RuO_2/TiO_2	P25
k_{app} MO (min^{-1})	0.032	0.065	0.049	0.039	0.023	0.033
k_{app} MB (min^{-1})	0.101	0.239	0.192	0.165	0.081	0.101

[a]This study. [b]According to ref 21.

% RuO_2/TiO_2 nanocatalyst showed the highest photocatalytic activity in the photocatalytic decomposition of MO with an apparent degradation rate constant reaching 0.065 min^{-1}, 2 times higher than that obtained with commercial TiO_2 P25.

The photocatalytic activity of the various heterostructures was also determined in the hydrogen (H_2) evolution from a methanol/water mixture (Figure 6). As evidenced in Figure 6A, the H_2 production after 3 h under UV irradiation was only 20.4 mL without photocatalysts, whereas in the absence of methanol but in the presence of catalysts, the evolved H_2 resulted in 24.5 mL. In contrast, the H_2 production was increased more than 77 times in the presence of the photocatalyst (5 wt % RuO_2/TiO_2) and methanol. These results revealed that both photocatalysts and sacrificial agent are required for an effective photocatalytic H_2 production. The time-course of the photocatalytic gas evolution over TiO_2 and RuO_2/TiO_2 containing different amounts of RuO_2 is shown in Figure 6B. The amount of the evolved gas almost linearly increased with increasing irradiation

time. The gas mixture mainly contained H_2 along with a small amount of carbon dioxide (CO_2), in an amount of 0.31 volume % but without any oxygen (O_2) and methane (CH_4) traces. As far as the hydrogen production is concerned (Figure 6C), the yield of H_2 over heterostructure RuO_2/TiO_2 photocatalysts was higher than that obtained over pure TiO_2 and commercial TiO_2 P25, whatever the RuO_2 content. As a consequence, the presence of RuO_2 played a key role in photocatalytic H_2 production.

To get a deeper insight in this issue, the influence of the RuO_2 loading on the photocatalytic H_2 production was studied (Figure 6D). It can be clearly seen that the rate of H_2 production increased initially by increasing the RuO_2 content, reached a maximum and then started to decrease once the RuO_2 content reached a certain value. Increasing the RuO_2 content from 1 to 5 wt %, the H_2 production rate increased from 441 to 618 μmol/h, the 5 wt % RuO_2/TiO_2 nanocatalyst yielding the highest rate of H_2 production. In contrast, with further increase in RuO_2 content from 5 to 10 wt %, the H_2 production rate dropped rapidly from 618 to 353 μmol/h.

3.3. Mechanistic Investigations. Introduction of RuO_2 clearly enhanced the photocatalytic properties of TiO_2 for both photodecomposition of organic dye and hydrogen production. As the textural properties (S_{BET} and mesoporosity) of all the nanocomposites studied are similar, the effect is related to better charge separation, as a consequence of suitable band alignment previously shown by our UPS/XPS studies.[21] However, the optimum RuO_2 content strongly depends on the kind of photocatalytic reaction envisaged, values of 1 and 5 wt % having been determined for organic dye degradation and hydrogen production, respectively.

In order to study how the doping with RuO_2 affects the formation of the charge trapping centers upon UV excitation and, in turn, the photocatalytic activity of TiO_2, 1 wt % RuO_2/TiO_2, 2.5 wt % RuO_2/TiO_2, and 5 wt % RuO_2/TiO_2 nanocatalysts, ESR investigations were performed after UV irradiation at 130 K, either in vacuo ($p < 10^{-5}$ mbar) or in the presence of p (O_2) = 10 mbar. After irradiation under vacuum, pure TiO_2 nanocatalysts (TiO_2, Figure 7a) show broad and weak resonances at g = 1.976, attributable to Ti^{3+} centers (Ti^{3+}[II] species).[31] No Ti^{3+} species are instead detectable in 1 wt % RuO_2/TiO_2 anatase nanocrystals (Figure 7b). Increasing the percentage of RuO_2 (2.5 wt % RuO_2/TiO_2, Figure 7c), the spectrum displays the presence of higher field features assigned to electrons trapped at two different Ti^{3+} centers: species [I],
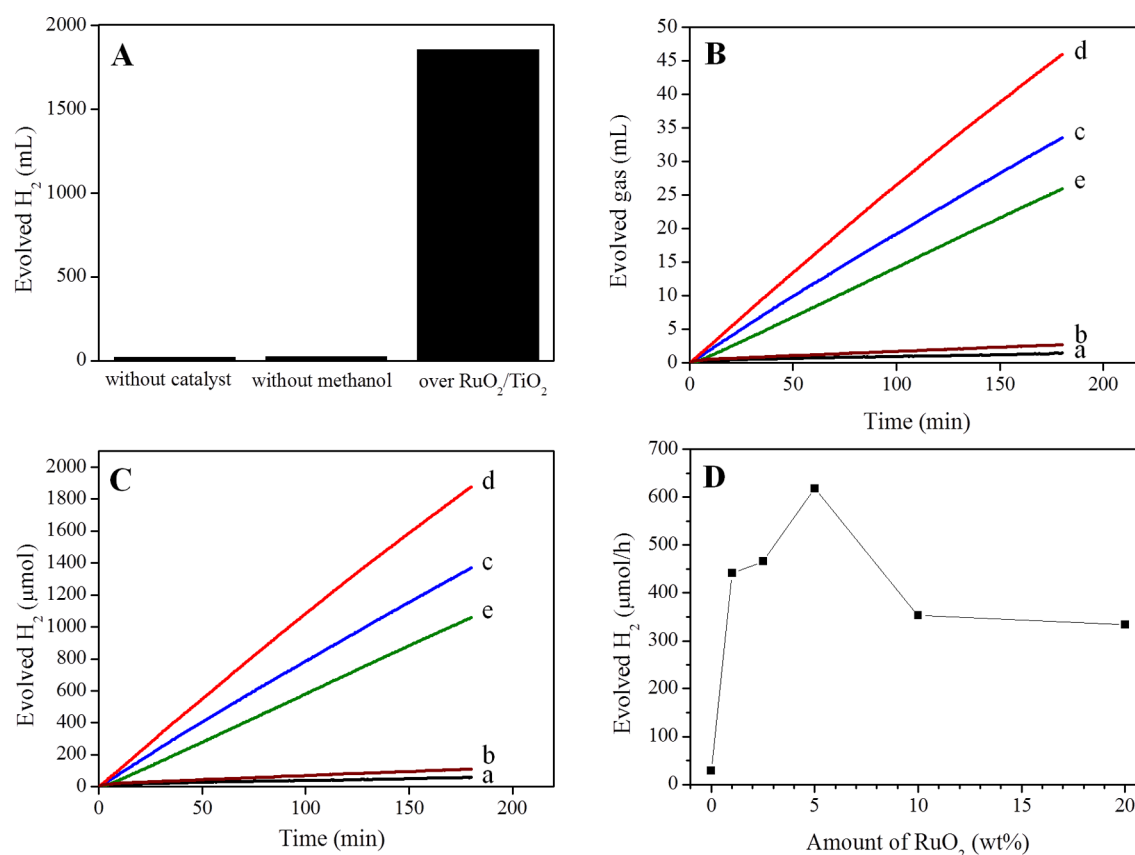
Figure 6. (A) Photocatalytic evolution of H$_2$ under different conditions, photocatalytic evolution of (B) gas and (C) H$_2$ over TiO$_2$ (a, black), P25 (b, wine), 1 wt % RuO$_2$/TiO$_2$ (c, blue), 5 wt % RuO$_2$/TiO$_2$ (d, red), and 10 wt % RuO$_2$/TiO$_2$ (e, olive) photocatalysts and (D) effect of RuO$_2$ loading on the H$_2$ production. All the experiments were run for 3 h under identical conditions (see experimental).
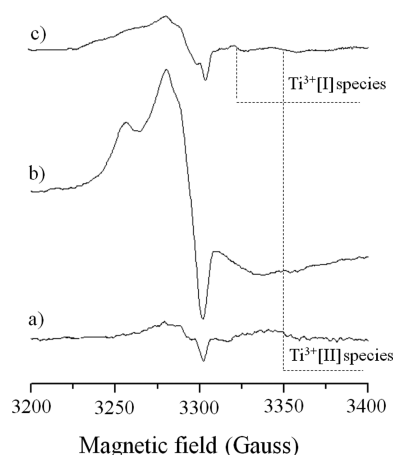

Figure 7. Experimental ESR spectra at 130 K after UV irradiation in vacuum ($p < 10^{-5}$ mbar) of (a) TiO$_2$, (b) 1 wt % RuO$_2$/TiO$_2$, (c) 2.5 wt % RuO$_2$/TiO$_2$, and (d) 5 wt % RuO$_2$/TiO$_2$ nanocrystals. Dashed lines highlight the signals attributed to Ti^{3+} species.

attributable to Ti^{3+} centers in a ordered crystalline environment, and species [II], broader and weaker, ascribable to Ti^{3+} centers located in a disordered environment and probably near to the surface.[31] The g values of these species are reported in Table 2. At highest Ru concentration (5 wt % RuO$_2$/TiO$_2$, Figure 7d), Ti^{3+} species are no more attributable.

The intense resonances at lower fields (Figure 7) can be attributed to coexisting oxygen species, O$^-$ and O$_2^-$,[32,33] whose g values and relative contributions have been calculated by

signal simulation (Table 2). In particular, Figure 8 reports the deconvolutions of the ESR signals of 1 wt % RuO$_2$/TiO$_2$ (Figure 8a) and 2.5 wt % RuO$_2$/TiO$_2$ (Figure 8b) samples. The presence of O$_2^-$ species, mainly occurring in 2.5 wt % RuO$_2$/TiO$_2$ nanocrystals, even when UV irradiation was performed under vacuum, may be related to the evolution of residuals OH$^-$ groups according to the following mechanism:[34]

$$h^+ + OH^- \rightarrow {}^{\bullet}OH \tag{1}$$

$$2{}^{\bullet}OH \rightarrow H_2O_2 \tag{2}$$

$$H_2O_2 + h^+ \rightarrow O_2^- + 2H^+ \tag{3}$$

$$O_2^- + h^+ \rightarrow O_2 \tag{4}$$

Considering their determinant role in oxidative catalysis (see below), the relative contribution of the O$^-$ species (calculated as % of the total intensity of the O$^-$ + O$_2^-$ signals) was determined and reported in Table 2.

The abundance and the stability of the paramagnetic centers detected by ESR after UV irradiation is relatable to the charge separation and to their inhibited recombination.[31−33,35] Hence, as already suggested in our previous studies,[31,35] the amount of hole trapping centers can be associated with the efficiency of the photocatalytic processes.

In the present case, from the area of integrated signals obtained after photoexcitation in vacuum, the concentration of holes trapped on O$^-$ centers always exceeds that of electrons trapped on Ti^{3+} centers. In particular, when plotted against the apparent reaction rate constant (k_{app}) for the degradation of
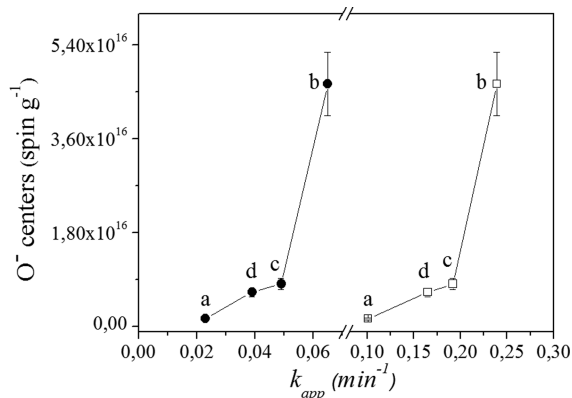
Table 2. g Tensor Values of the Paramagnetic Defects Detected after Photoexcitation in Vacuum ($p < 10^{-5}$ mbar) in TiO$_2$ and TiO$_2$/RuO$_2$ Nanocrystals, Determined by Simulation of the ESR Features[a]

photocatalyst	O$^-$ centers (%)	O$^-$ species	Ti^{3+} species	O$_2^-$ species
TiO$_2$	100%	g⊥ = 2.0129, g∥ = 2.0047	g⊥ ∼ 1.976, g∥ = n.d.	−
1 wt % RuO$_2$−TiO$_2$	50%	g⊥ = 2.0100, g∥ = 2.0028	−	g$_{zz}$ = 2.0286, g$_{yy}$ = 2.0096, g$_{xx}$ = 2.0003
2.5 wt % RuO$_2$−TiO$_2$	27%	g⊥ = 2.0129, g∥ = 2.0036	Ti^{3+}[I]: g⊥ = 1.9880, g∥ = n.d. Ti^{3+}[II]: g⊥ ∼ 1.976, g∥ = n.d.	O$_2^-$[I]: g$_{zz}$ = 2.0258, g$_{yy}$ = 2.0110, g$_{xx}$ = 1.9999 O$_2^-$[II]: g$_{zz}$ = 2.0339, g$_{yy}$ = 2.0099, g$_{xx}$ = 2.0000
5 wt % RuO$_2$−TiO$_2$	60%	g⊥ = 2.0129, g∥ = 2.0047	n.d.	−

[a]The relative contribution of the O$^-$ species (calculated as % of the total intensity of the O$^-$ + O$_2^-$ signals) is also reported.
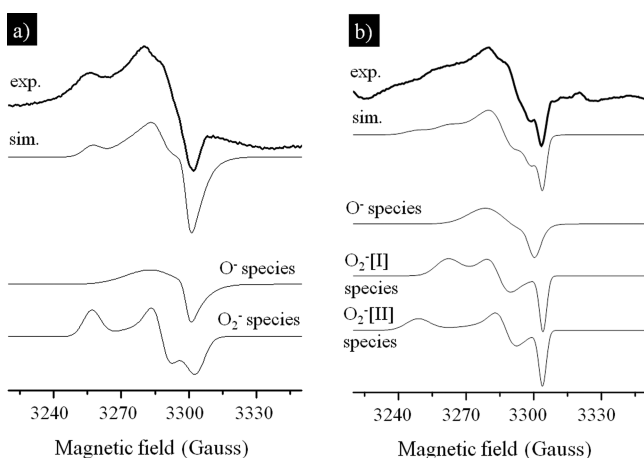
Figure 8. (a) Deconvolution (sim.) of ESR signals of 1 wt % RuO$_2$/TiO$_2$ nanoparticles (exp.) into O$^-$ and O$_2^-$ species. (b) Deconvolution (sim.) of ESR signals of 2.5 wt % RuO$_2$/TiO$_2$ nanoparticles (exp.) into O$^-$ and O$_2^-$ species.

MB and of MO,[21] the amount of O$^-$ centers increases with the k_{app} increase [i.e., with the increase of photoefficiency (Figure 9), becoming the highest for 1 wt % RuO$_2$/TiO$_2$]. This trend suggests a parallelism between the photoactivity of nanocrystals and the amount of trapped holes which ultimately drives the surface photooxidation processes. On the contrary, considering also their low amount, no simple relation between the
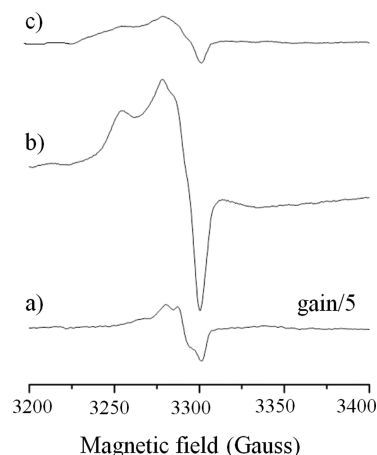
abundance of Ti^{3+} centers and the photoactivity can be suggested.

These outcomes support the idea that the formation of TiO$_2$/RuO$_2$ heterojunctions promotes a more efficient electron−hole separation which results, in turn, in an increase of the photocatalytic activity. However, it is also worth mentioning that the photoefficiency in the MB or MO degradation gradually decreased with increasing RuO$_2$ concentration (k_{app} 5 wt % RuO$_2$/TiO$_2$ < k_{app} 2.5 wt % RuO$_2$/TiO$_2$ < k_{app} 1 wt % RuO$_2$/TiO$_2$). This behavior may be attributed to the possible action of RuO$_2$ as charge recombination center, when deposited in a higher amount on titania.[19] As it has been previously reported that the conductivity of TiO$_2$/RuO$_2$ heterostructures is higher than that of bare TiO$_2$, a more rapid charge transfer and recombination in RuO$_2$ can be suggested.[36]

To further elucidate the mechanism of the MB and MO photooxidative processes, ESR studies on TiO$_2$, 1 wt % RuO$_2$/TiO$_2$, 2.5 wt % RuO$_2$/TiO$_2$, and 5 wt % RuO$_2$/TiO$_2$ nanocrystals were carried out after UV irradiation at 130 K in the presence of $p(O_2)$ = 10 mbar and subsequent removal of the residual oxygen by evacuation at $p < 10^{-5}$ mbar.

After the oxygen contact (Figure 10), the resonances of O$_2^-$ centers can be easily detected. In particular, it can be observed that the amount of superoxide species formed is higher in 1 wt % RuO$_2$/TiO$_2$, 2.5 wt % RuO$_2$/TiO$_2$ and 5 wt % RuO$_2$/TiO$_2$ than in bare TiO$_2$ nanoparticles and raises as the k_{app} for the

Figure 9. Trend of the relative amounts of O$^-$ species calculated for different nanocatalysts vs apparent reaction rate constant (k_{app}) for the degradation of MB (□) and MO (●). (a) TiO$_2$, (b) 1 wt % RuO$_2$/TiO$_2$, (c) 2.5 wt % RuO$_2$/TiO$_2$, and (d) 5 wt % RuO$_2$/TiO$_2$.

Figure 10. ESR spectra at 130 K after UV irradiation in the presence of 10 mbar of O$_2$ and then vacuum at $p < 10^{-5}$ mbar of (a) TiO$_2$, (b) 1 wt % RuO$_2$/TiO$_2$, (c) 2.5 wt % RuO$_2$/TiO$_2$, and (d) 5 wt % RuO$_2$/TiO$_2$ nanocatalysts.

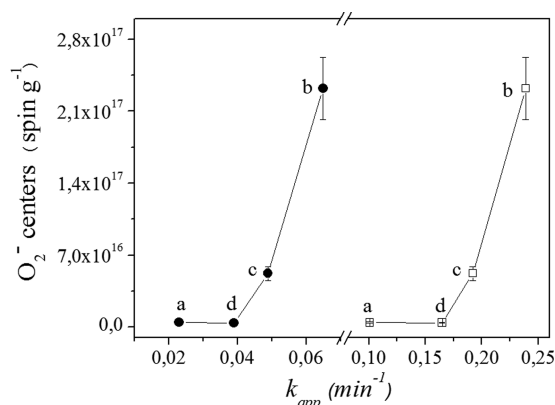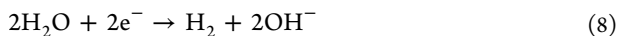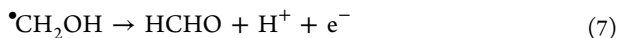degradation of MB and MO increases (Figure 11). This trend on one hand indicates an indirect involvement of these
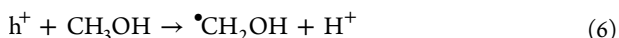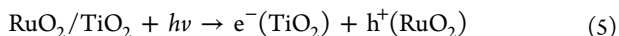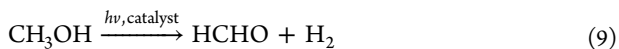

Figure 11. Trend of the abundance of superoxide species (O_2^-) as a function of apparent reaction rate constant (k_{app}) for the degradation of MB ($\square$) and MO ($\bullet$). (a) TiO_2, (b) 1 wt % RuO_2/TiO_2, (c) 2.5 wt % RuO_2/TiO_2, and (d) 5 wt % RuO_2/TiO_2 nanocatalysts.

paramagnetic species in the photooxidative processes, and on the other, it confirms that the creation of TiO_2/RuO_2 heterojunctions effectively improves the charge separation, boosting the photoefficiency of RuO_2 doped nanocrystals.
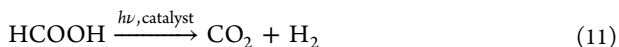
As far as the hydrogen production by methanol photoreforming with these nanocomposites is concerned, the experimental conditions used suggest the following mechanism for H_2 generation. In the absence of oxygen and presence of sacrificial species such as methanol, the holes generated by the light (eq 5) react with methanol (CH_3OH) to produce the $^\bullet CH_2OH$ radical. The $^\bullet CH_2OH$ radical possesses sufficiently negative oxidation potential (-0.74 V) and could further react to produce H^+, electron and HCHO (eq 6).[37,38] On the other hand, electrons in the conduction band of the particle will simultaneously reduce water or protons in the solution to form gaseous H_2 as shown by eq 7. These reactions proceed competitively with the recombination of the photoinduced electrons and holes.

$$RuO_2/TiO_2 + h\nu \rightarrow e^-(TiO_2) + h^+(RuO_2) \tag{5}$$

$$h^+ + CH_3OH \rightarrow {}^\bullet CH_2OH + H^+ \tag{6}$$

$${}^\bullet CH_2OH \rightarrow HCHO + H^+ + e^- \tag{7}$$

$$2H_2O + 2e^- \rightarrow H_2 + 2OH^- \tag{8}$$

As a result, the overall reaction is

$$CH_3OH \xrightarrow{h\nu,\text{catalyst}} HCHO + H_2 \tag{9}$$

Formaldehyde (HCHO) obtained can be further oxidized to formic acid HCOOH and subsequently to CO_2 along with hydrogen generation according to

$$HCHO + H_2O \xrightarrow{h\nu,\text{catalyst}} HCOOH + H_2 \tag{10}$$

$$HCOOH \xrightarrow{h\nu,\text{catalyst}} CO_2 + H_2 \tag{11}$$

This mechanism points out the pivotal role of h^+ species in enhancing the photo-oxidation of methanol and, consequently, the hydrogen production. As assessed by ESR investigation after photoexcitation in vacuum, the amount of hole traps (i.e.,

O^- centers) is higher for RuO_2/TiO_2 nanocatalysts than for pure TiO_2. This highlights the role of RuO_2 in stabilizing the photogenerated holes and explains the better ability of the heterojunctions in the hydrogen production. A second key factor favoring H_2 production with RuO_2/TiO_2 nanocatalysts is the Schottky barriers developed at the interface between RuO_2 and TiO_2. Thus, postulating an idealized mechanistic scheme of electron−hole pair separation of a well-defined planar metal−semiconductor contact, our previous XPS studies clearly showed a favorable upward band bending at the interface of the RuO_2/TiO_2 heterojunction, the phenomenon increasing with the RuO_2 amount.[21] As a result, the enhanced H_2 production rate with increasing the RuO_2 loading up to 5 wt % can be due to a higher number of Schottky barriers at the RuO_2/TiO_2 interfaces. However, above a certain RuO_2 amount, the active sites on the TiO_2 surface that were available for absorption of light and electron donors can be covered by excessive RuO_2 particles inhibiting the photocatalytic processes. Moreover, as mentioned above, RuO_2 nanoparticles in composites containing higher RuO_2 loadings may act as recombination centers for photogenerated electrons and holes. Both phenomena are likely at the origin of the significant decrease in photocatalytic activity for RuO_2 loadings higher than 5 wt %.

At this stage, it is worth underlining that changes in morphology and size-dependent electronic properties should also be taken into account to rationalize the photocatalytic properties on the basis of band bending at the RuO_2/TiO_2 interface. Indeed, our previous studies showed that the observed band bending in the RuO_2/TiO_2 nanocatalysts is smaller than in a well-defined planar metal−semiconductor contact. Indeed, the small size of both TiO_2 and RuO_2 particles does not allow for the saturation of the band bending as the standard space charge layers thickness will exceed the size of the particles (an effect which depends on doping). Furthermore, the spatial distribution of the RuO_2 deposits on the TiO_2 substrates are not yet optimized, high RuO_2 loadings hampering a favorable vectorial charge separation. As a consequence, further efforts are required to better control the RuO_2 nanoparticules distribution over TiO_2 in order to produce highly efficient RuO_2/TiO_2 heterostructures.

4. CONCLUSION

In summary, mesoporous heterostructure RuO_2/TiO_2 nanoparticles photocatalysts showed enhanced photocatalytic activity in organic dye decomposition and H_2 production by methanol photoreforming compared to pure TiO_2 and commercial P25. For both kinds of photocatalytic reactions, different optimum RuO_2 loadings have been evidenced. Thus, heterojunction 1 wt % RuO_2/TiO_2 photocatalyst showed the highest rates for the degradation of MB and MO dyes under UV light irradiation. These findings were rationalized on the basis of ESR studies that evidenced the higher amount of trapped holes for the 1 wt % RuO_2/TiO_2 photocatalyst and the role of superoxide paramagnetic species in the photodecomposition of organic dyes. On the other hand, heterojunction 5 wt % RuO_2/TiO_2 photocatalysts showed the highest catalytic activity with average hydrogen production rate of 618 μmol h^{-1}, the latter decreasing dramatically to 29 μmol h^{-1} without RuO_2 that points out the key role of RuO_2 for efficient hydrogen production. Favorable band bending at the RuO_2/TiO_2 interface and key role of photogenerated holes have been underlined to explain the highest activity of the

RuO_2/TiO_2 photocatalysts for hydrogen production. Further efforts are currently in progress to achieve a better control of the RuO_2 nanoparticle distribution in order to reach optimum vectorial charge distribution and enhanced photocatalytic hydrogen production rates. The overall results support that understanding how the cooperative interaction between RuO_2 and TiO_2 affects the formation and reactivity of charge trapping centers may lay the groundwork for the development of highly active photocatalysts.

■ ASSOCIATED CONTENT

Ⓢ Supporting Information

Additional figures concerning N_2 sorption (2.5 wt % RuO_2–TiO_2), XPS (2.5 and 10 wt % RuO_2–TiO_2) and photocatalytic studies (MO photodegradation as a function of the RuO_2 loading). This material is available free of charge via the Internet at http://pubs.acs.org.

■ AUTHOR INFORMATION

Corresponding Author

*E-mail: t.toupance@ism.u-bordeaux1.fr. Tel: 33 (0)5 40 00 25 23.

Notes

The authors declare no competing financial interest.

■ ACKNOWLEDGMENTS

■ REFERENCES

(1) Hoffmann, M. R.; Martin, S. T.; Choi, W.; Bahnemann, D. W. Environmental Applications of Semiconductor Photocatalysis. *Chem. Rev.* **1995**, *95*, 69–96.

(2) Ravelli, D.; Dondi, D.; Fagnoni, M.; Albini, A.; Photocatalysis, A. Multi-Faceted Concept for Green Chemistry. *Chem. Soc. Rev.* **2009**, *38*, 1999–2011.

(3) Yu, C.; Li, G.; Kumar, S.; Yang, K.; Jin, R. Phase Transformation Synthesis of Novel Ag_2O/Ag_2CO_3 Heterostructures with High Visible Light Efficiency in Photocatalytic Degradation of Pollutants. *Adv. Mater.* **2014**, *26*, 892–898.

(4) Fujishima, A.; Rao, T. N.; Tryk, D. A. Titanium Dioxide Photocatalysis. *J. Photochem. Photobiol., C* **2000**, *1*, 1–21.

(5) Logar, M.; Jancar, B.; Sturm, S.; Suvorov, D. Weak Polyion Multilayer-Assisted in situ Synthesis as a Route Toward a Plasmonic Ag/TiO_2 Photocatalyst. *Langmuir* **2010**, *26*, 12215–12224.

(6) Zhang, X.; Zhou, M.; Lei, L. Preparation of an $Ag-TiO_2$ Photocatalyst Coated on Activated Carbon by MOCVD. *Mater. Chem. Phys.* **2005**, *91*, 73–79.

(7) Chen, X.; Zhu, H. Y.; Zhao, J. C.; Zheng, Z. F.; Gao, X. P. Visible-Light-Driven Oxidation of Organic Contaminants in Air with Gold Nanoparticle Catalysts on Oxide Supports. *Angew. Chem., Int. Ed.* **2008**, *47*, 5353–5356.

(8) Fang, J.; Cao, S. W.; Wang, Z.; Shahjamali, M. M.; Loo, S. C. J.; Barber, J.; Xue, C. Mesoporous Plasmonic $Au–TiO_2$ Nanocomposites for Efficient Visible-Light-driven Photocatalytic Water Reduction. *Int. J. Hydrogen Energy* **2012**, *37*, 17853–17861.

(9) Liu, Z.; Sun, D. D.; Guo, P.; Leckie, J. O. An Efficient Bicomponent TiO_2/SnO_2 Nanofiber Photocatalyst Fabricated by Electrospinning with a Side-by-Side Dual Spinneret Method. *Nano Lett.* **2007**, *7*, 1081–1085.

(10) Zhang, R.; Wu, H.; Lin, D.; Pan, W. Photocatalytic and Magnetic Properties of the $Fe-TiO_2/SnO_2$ Nanofiber via Electrospinning. *J. Am. Ceram. Soc.* **2010**, *93*, 605–608.

(11) Cavas, M.; Gupta, R. K.; Al-Ghamdi, A. A.; Serbetci, Z.; Gafer, Z. H.; El-Tantawy, F.; Yakuphanoglu, F. Fabrication and Electrical Characterization of Solution-processed All-Oxide Transparent NiO/TiO_2 p-n Junction Diode by Sol-Gel Spin Coating Method. *J. Electroceram.* **2013**, *31*, 260–264.

(12) Iwaszyk, A.; Nilan, M.; Jin, Q.; Fujishima, M.; Tada, H. Origin of the Visible-Light Response of Nickel(II) Oxide Cluster Surface Modified Titanium(IV) Dioxide. *J. Phys. Chem. C* **2013**, *117*, 2709–2718.

(13) Dalven, R. Physics of Metal–Semiconductor and Metal–Insulator–Semiconductor Junctions, Introduction to Applied Solid State Physics, 2nd ed.; Plenum Press: New York, 1990, Chapter 4; pp 111–128.

(14) Glassford, K. M.; Chelikowsky, J. R. Electron Transport Properties in RuO_2 Rutile. *Phys. Rev. B: Condens. Matter Mater. Phys.* **1994**, *49*, 7107–7114.

(15) Hartmann, A. J.; Neilson, M.; Lamb, R. N.; Watanabe, K.; Scott, J. F. Ruthenium Oxide and Strontium Ruthenate Electrodes for Ferroelectric Thin-films Capacitors. *Appl. Phys. A: Mater. Sci. Process.* **2000**, *70*, 239–242.

(16) Schafranek, R.; Schaffner, J.; Klein, A. In Situ Photoelectron Study of the $(Ba,Sr)TiO_3/RuO_2$ Contact Formation. *J. Eur. Ceram. Soc.* **2010**, *30*, 187–192.

(17) Chueh, Y. L.; Hsieh, C. H.; Chang, M.T.; Chou, Li. J.; Lao, C. S.; Song, J. H.; Gan, J. Y.; Wang, Z. L. RuO_2 Nanowires and RuO_2/TiO_2 Core/Shell Nanowires: From Synthesis to Mechanical, Optical, Electrical, and Photoconductive Properties. *Adv. Mater.* **2007**, *19*, 143–149.

(18) Seitsonen, A. P.; Over, H. Oxidation of HCl over TiO_2-Supported RuO_2: A Density Functional Theory Study. *J. Phys. Chem. C* **2010**, *114*, 22624–22629.

(19) Ismail, A. A.; Robben, L.; Bahnemann, D. W. Study of the Efficiency of UV and Visible-Light Photocatalytic Oxidation of Methanol on Mesoporous $RuO_2–TiO_2$ Nanocomposites. *ChemPhysChem* **2011**, *12*, 982–991.

(20) Kundu, S.; Vidal, A. B.; Yang, F.; Ramirez, P. J.; Senanayake, D. D.; Stacchiola, D.; Evans, J.; Liu, P.; Rodriguez, J. A. Special Chemical Properties of RuO_x Nanowires in $RuO_x/TiO_2(110)$: Dissociation of Water and Hydrogen Production. *J. Phys. Chem. C* **2012**, *116*, 4767–4773.

(21) Uddin, Md. T.; Nicolas, Y.; Olivier, C.; Toupance, T.; Müller, M. M.; Kleebe, H.-J.; Rachut, K.; Ziegler, J.; Klein, A.; Jaegermann, W. Preparation of RuO_2/TiO_2 Mesoporous Heterostructures and Rationalization of Their Enhanced Photocatalytic Properties by Band Alignment Investigations. *J. Phys. Chem. C* **2013**, *117*, 22098–22110.

(22) Tebby, Z.; Babot, O.; Toupance, T.; Park, D. H.; Campet, G.; Delville, M. H. Low-temperature UV-Processing of Nanocrystalline Nanoporous Thin TiO_2 Films: An Original Route toward Plastic Electrochromic Systems. *Chem. Mater.* **2008**, *20*, 7260–7267.

(23) Cojocaru, L.; Olivier, C.; Toupance, T.; Sellier, E.; Hirsch, L. Size and Shape Fine-Tuning of SnO_2 Nanoparticles for Highly Efficient and Stable Dye-Sensitized Solar Cells. *J. Mater. Chem. A* **2013**, *1*, 13789–13799.

(24) Ensling, D.; Thissen, A.; Gassenbauer, Y.; Klein, A.; Jaegermann, W. In-situ Preparation and Analysis of Functional Oxides. *Adv. Eng. Mater.* **2005**, *7*, 945–949.

(25) Adamski, A.; Spalek, T.; Sojka, Z. Application of EPR Spectroscopy for Elucidation of Vanadium Speciation in VO_x/ZrO_2 Catalyst Subject to Redox Treatment. *Res. Chem. Intermed.* **2003**, *29*, 793–804.

(26) Rouquerol, F.; Rouquerol, J.; Sing, K. *Adsorption by Powders & Porous Solids*; Academic Press: New York, 1999; pp 19–20.

(27) Leofanti, G.; Padovan, M.; Tozzola, G.; Venturelli, B. Surface Area and Pore Texture of Catalysts. *Catal. Today* **1998**, *41*, 207–219.

(28) Qadir, K.; Joo, S. H.; Mun, B. S.; Butcher, D. R.; Renzas, J. R.; Aksoy, F.; Liu, Z.; Somorjai, G. A.; Park, J. Y. Intrinsic Relation

between Catalytic Activity of CO Oxidation on Ru Nanoparticles and Ru Oxides Uncovered with Ambient Pressure XPS. *Nano Lett.* **2012**, *12*, 5761−5768.

(29) Södergren, S.; Siegbahn, H.; Rensmo, H.; Lindström, H.; Hagfeldt, A.; Lindquist, S.-E. Lithium Intercalation in Nanoporous Anatse TiO$_2$ Studied with XPS. *J. Phys. Chem. B* **1997**, *101*, 3087−3090.

(30) Guo, Y.; Wang, H.; He, C.; Qiu, L.; Cao, X. Uniform Carbon-Coated ZnO Nanorods: Microwave-Assisted Preparation, Cytotoxicity, and Photocatalytic Activity. *Langmuir* **2009**, *25*, 4678−4684.

(31) Scotti, R.; Bellobono, I. R.; Canevali, C.; Cannas, C.; Catti, M.; D'Arienzo, M.; Musinu, A.; Polizzi, S.; Sommariva, M.; Testino, A.; Morazzoni, F. Sol-Gel Pure and Mixed-Phase Titanium Dioxide for Photocatalytic Purposes: Relations between Phase Composition, Catalytic Activity, and Charge-Trapped Sites. *Chem. Mater.* **2008**, *20*, 4051−4061.

(32) Berger, T.; Diwald, O.; Knozinger, E.; Sterrer, M.; Yates, J. T. UV Induced Local Heating Effects in TiO$_2$ Nanocrystals. *Phys. Chem. Chem. Phys.* **2006**, *8*, 1822−1826.

(33) Carter, E.; Carley, A. F.; Murphy, D. M. Evidence for O$_2^-$ Radical Stabilization at Surface Oxygen Vacancies on Polycrystalline TiO$_2$. *J. Phys. Chem. C* **2007**, *111*, 10630−10638.

(34) Howe, R. F.; Gratzel, M. EPR Study of Hydrated Anatase under UV Irradiation. *J. Phys. Chem.* **1987**, *91*, 3906−3909.

(35) D'Arienzo, M.; Carbajo, J.; Bahamonde, A.; Crippa, M.; Polizzi, S.; Scotti, R.; Wahba, L.; Morazzoni, F. Photogenerated Defects in Shape-Controlled TiO$_2$ Anatase Nanocrystals: A Probe to Evaluate the Role of Crystal Facets in Photocatalytic Processes. *J. Am. Chem. Soc.* **2011**, *133*, 17652−17661.

(36) Blondeel, G.; Harriman, A.; Porter, G.; Urwin, D.; Kiwi, J. Design, Preparation, and Characterization of RuO$_2$/TiO$_2$ Colloidal Catalytic Surfaces Active in Photooxidation of Water. *J. Phys. Chem.* **1983**, *87*, 2629−2636.

(37) Perissinotti, L. L.; Brusa, M. A.; Grela, M. A. Yield of Carboxyl Anion Radicals in the Photocatalytic Degradation of Formate over TiO$_2$ Particles. *Langmuir* **2001**, *17*, 8422−8427.

(38) Schneider, J.; D. W. Bahnemann, D. W. Undesired Role of Sacrificial Reagents in Photocatalysis. *J. Phys. Chem. Lett.* **2013**, *4*, 3479−3483.